HHS Public Access

Author manuscript

Biofabrication. Author manuscript; available in PMC 2022 January 21.

Published in final edited form as:

Biofabrication. ; 13(1): . doi:10.1088/1758-5090/abc1be.

Toward a neurospheroid niche model: optimizing embedded 3D bioprinting for fabrication of neurospheroid brain-like co-culture constructs

Yi-Chen Ethan Li[#1,2], **Yasamin A Jodat**[#1,3], **Roya Samanipour**[#1,4], **Giulio Zorzi**[1], **Kai Zhu**[1,5], **Minoru Hirano**[1,6], **Karen Chang**[7], **Adnan Arnaout**[1], **Shabir Hassan**[1], **Navneet Matharu**[8,9], **Ali Khademhosseini**[1,10,11,12,13], **Mina Hoorfar**[4,15], **Su Ryon Shin**[1,15]

[1]Division of Engineering in Medicine, Department of Medicine, Brigham and Women's Hospital, Harvard Medical School, Boston, MA 02139, United States of America

[2]Department of Chemical Engineering, Feng Chia University, Taichung 40724, Taiwan

[3]Department of Mechanical Engineering, Stevens Institute of Technology, New Jersey 07030, United States of America

[4]School of Engineering, University of British Columbia, Kelowna V1V 1V7, BC, Canada

[5]Department of Cardiac Surgery, Zhongshan Hospital Fudan University, Shanghai 200032, China

[6]Future Vehicle Research Department, Toyota Research Institute North America, Toyota Motor North America Inc. 1555 Woodridge Ave, Ann Arbor, MI 48105, United States of America

[7]Graduate Institute of Clinical Dentistry, School of Dentistry, National Taiwan University, Taiwan

[8]Department of Bioengineering and Therapeutic Sciences, University of California San Francisco, San Francisco, California 94158, United States of America

[9]Institute for Human Genetics, University of California, San Francisco, CA 94158, United States of America

[10]Department of Bioengineering, Henry Samueli School of Engineering and Applied Sciences, University of California-Los Angeles, Los Angeles, California 90095, United States of America

[11]Center for Minimally Invasive Therapeutics (C-MIT), University of California-Los Angeles, Los Angeles, California 90095, United States of America

[12]Department of Chemical and Biomolecular Engineering, Henry Samueli School of Engineering and Applied Sciences, University of California–Los Angeles, Los Angeles, California 90095, United States of America

[15]Authors to whom any correspondence should be addressed. sshin4@bwh.harvard.edu.

Author contributions

The manuscript was written through contributions of all authors. All authors have given approval to the final version of the manuscript. Yi Chen Ethan Li, Yasamin A Jodat and Roya Samanipour contributed equally as first authors.

Supplementary material for this article is available online

Conflicts of interest

The authors declare no conflicts of interest.

[13]Department of Radiology, David Geffen School of Medicine, University of California-Los Angeles, Los Angeles, CA 90095, United States of America

[#] These authors contributed equally to this work.

Abstract

A crucial step in creating reliable *in vitro* platforms for neural development and disorder studies is the reproduction of the multicellular three-dimensional (3D) brain microenvironment and the capturing of cell-cell interactions within the model. The power of self-organization of diverse cell types into brain spheroids could be harnessed to study mechanisms underlying brain development trajectory and diseases. A challenge of current 3D organoid and spheroid models grown in petri-dishes is the lack of control over cellular localization and diversity. To overcome this limitation, neural spheroids can be patterned into customizable 3D structures using microfabrication. We developed a 3D brain-like co-culture construct using embedded 3D bioprinting as a flexible solution for composing heterogenous neural populations with neurospheroids and glia. Specifically, neurospheroid-laden free-standing 3D structures were fabricated in an engineered astrocyte-laden support bath resembling a neural stem cell niche environment. A photo-crosslinkable bioink and a thermal-healing supporting bath were engineered to mimic the mechanical modulus of soft tissue while supporting the formation of self-organizing neurospheroids within elaborate 3D networks. Moreover, bioprinted neurospheroid-laden structures exhibited the capability to differentiate into neuronal cells. These brain-like co-cultures could provide a reproducible platform for modeling neurological diseases, neural regeneration, and drug development and repurposing.

Keywords

embedded bioprinting; neural stem cells; astrocytes; neurospheroids; thermal-healing hydrogels; brain tissues

1. Introduction

Modeling neural stem cell niches in two-dimensional (2D) petri-dishes poses challenges as these platforms do not accurately recapitulate the complex biological behavior of the native 3D brain tissue and lack the functional aspects of 3D cell-cell interactions. This limitation has posed a significant obstacle for effective drug screening for many neurodevelopmental disorders or neuronal regeneration cases. The neural stem cell niche in the adult brain is structured through astrocytes around neuroblast clusters [1]. Within the neural stem cell niche, neuroblasts are formed locally and migrate to farther zones to enable cell-cell interactions and to receive inputs to maintain structural diversity [2]. Moreover, the activity and neuronal differentiation of neuroblasts in the brain's stem cell niche is achieved through co-administration of non-neural supporting cells such as astrocytes [3]. Therefore, to better understand these multicellular mechanisms and events underlying the activation of the neural stem cell niche, it is essential to capture higher levels of the brain tissue's intricacies in niche models using programmable structural heterogeneity and patternable 3D structures.

Over the past decade, 3D brain models made up of spheroids and organoids have shown outstanding potential for creating anatomically relevant arrangements of heterogenous cellular networks in 3D matrices [4–6]. In such systems, an aggregation of stem cells can be cultured over a period of a few months to allow for the differentiation and self-organization of these cells into brain organoids [7]. For instance, Lancaster *et al* [8] and Pasca *et al* [9] developed human pluripotent stem cell-derived cerebral micro-organoids capable of recapitulating the human cortical development to obtain human brain-like tissues. Accordingly, the development of a 3D biomimetic human brain model containing both neurons and neuroglia was indicated as a strong requisite for replicating some of the main cell-cell interactions in the brain, namely, astrocyte-neuron interactions. To understand the functions and interactions which occur in the developing brain, a variety of research platforms have been developed based on engineering microfabrication techniques such as 3D patterned micro-grooves, photolithography, and micro-molding [10]. For instance, Park *et al* fabricated a neurospheroid-based Alzheimer's model in a microfluidic chip with a constant fluid flow to mimic the fluids in the *in vivo* interstitial space of the brain microenvironment. Consequently, the effects at the interstitial level of diffusion-dominant flow on the removal of extracellular amyloid-β, a major factor contributing to Alzheimer's disease, could be evaluated using this neurospheroid-based microfluidic chip [11].

An effective approach to model specific brain regions with population diversity would be to design platforms where an assortment of organoids could be patterned into self-organizing interconnected structures which mimic specific brain regions. For instance, a recent study reported on interneuron migration *in vitro* via fusing region-specific organoids to recapitulate the developing brain's molecular dynamics [12]. Currently, this procedure principally relies on the self-assembly of such organoids, and thus involves high batch-to-batch variability [13]. Additive manufacturing techniques could be employed to pattern these structures to favor self-organization in a more controllable and reproducible manner. 3D embedded bioprinting is a novel strategy used to fabricate soft and self-supporting tissues, such as anisotropic directional nerve fiber tracts with expansive 3D configurations [14–16]. This method is based on the direct extrusion of a shear-thinning bioink into a thermal-healing supporting hydrogel matrix. As such, 3D geometries with controllable anisotropy and microstructures in a 3D space could easily be attained. The current state of embedded printing involves the use of a consolidating material, such as gelatin- [17], gellan microgel- [18], carbopol polymer- [19], and Pluronic-based [20] materials, to provide structural support and shape formation during the 3D printing process. Afterwards, the supporting polymer could either remain, to create and study spatial geometries and 3D interactions among the printed soft gels, or could otherwise be removed to give out stand-alone structures [15, 16, 21, 22]. Embedded bioprinting can thus give rise to augmented engineered tissues with further levels of detail and intricacy such as those found in a natural tissue.

Here, we used embedded 3D bioprinting to develop a soft brain-like co-culture construct containing neurospheroids and astrocytes within a mechanically engineered biomaterial to mimic the brain's stiffness. Specifically, we fabricated 3D neurospheroid patterns using a neural stem cell-laden bioink inside an astrocyte-laden thermal-healing supporting gel to provide a platform for controlling and directing the self-organization and differentiation of

neurospheroids in 3D matrices, which could be a convenient tool to study the interactions of early neurogenesis with neuroglia. As a proof of concept, we optimized the 3D embedded printing conditions for the fabrication of a neurospheroidastrocyte niche-like construct. Finally, by controlling the organization of high-level spheroids without perturbing their self-organization capabilities, as well as tuning the biophysical properties of the biomaterials (e.g. degradability and mechanical properties), we could achieve a brain-like tissue in a controlled manner and propose a robust platform as a neural stem cell niche.

2. Materials and methods

2.1. Materials

Dialysis membrane (Spectra/Por molecular porous membrane tubing, MWCO 12–14 000) was purchased from Fisher Scientific. The following were purchased from Sigma-Aldrich (St. Louis, MO, USA): Calcium chloride ($CaCl_2$), alginic acid sodium salt (from brown algae, low viscosity, 100–300 cP), methacrylic anhydride (MA), gelatin from porcine skin (type A, 300 Bloom), photo-initiator (PI, 2-hydroxy-1-[4-(2-hydroxyethoxy) phenyl]-2-methyl-1-propanone, Irgacure 2959), Triton-X 100, laminin from Engelbreth-Holm-Swarm murine sarcoma basement membrane, and poly-D-lysine hydrobromide (PDL).

2.2. GelMA synthesis

Synthesis of medium degree gelatin methacryloyl (GelMA) was done based on a previous protocol [23, 24]. In short, gelatin from porcine skin (10. w/v%) was dissolved in Dulbecco's phosphate-buffered saline (DPBS) at 50 °C followed by stirring at 240 rpm. was added to the solution drop by drop to make a 1.25. v/v% MA concentration. After 2 h at 50 °C with constant stirring, warm DPBS was added to the mixture at a 1:1 ratio. Next, the solution was allowed to be dialyzed in distilled (DI) water at 40 °C and 500 rpm over the course of 5 d. The DI water tank was refreshed every day. On day 6, the dialyzed GelMA solution was collected and stocked at −80 °C. Prior to use for experiments, the solution was freeze dried for 4 d.

2.3. Cell culture and neural differentiation

To isolate astrocytes, rat cortices were obtained from the carcasses of rats that were discarded after hearts had been expelled following protocols (Protocol #: 2016N000379) approved by the Institute's Committee on Animal Care [25]. Briefly, rat cortices were dissected, the hemispheres were cut into small pieces, incubated in Hank's balanced salt solution (HBSS, Gibco) and 2.5% trypsin, and centrifuged to obtain a pellet of cortex tissue pieces [26]. Through mechanical trituration, a suspension of dissociated cells was obtained. The astrocytes were cultured in Dulbecco's modified Eagle's medium (DMEM, Gibco) supplemented with 10% fetal bovine serum (FBS, Gibco) and 1% penicillin streptomycin (P/S, Gibco). Neuroepithelial (NE-4C, CRL-2925, ATCC) cells were cultured and expanded in Minimum Essential Medium Eagle (MEM, Thermo Fisher Scientific) supplemented with 10% FBS and 1% P/S. To induce neuronal differentiation, 1 μM retinoic acid (RA) was added to the NE-4C culture for 48 h and the cells were cultured in MEM, 1% Insulin-Transferrin-Selenium (ITS, Thermo Fisher Scientific), 2 mM L-glutamine (Thermo Fisher Scientific), and 1% P/S [27–29]. After this time, RA was removed and the culture was

continued in Neurobasal medium supplemented with B27 (Gibco). For 2D differentiation, the well plates were coated with PDL prior to differentiation induction. All cell cultures were passaged according to the protocol provided by the respective vendors.

2.4. Support bath preparation

The supporting hydrogel was developed by suspending astrocytes at a concentration of 8×10^6 cells ml^{-1} in a DMEM-based solution containing calcium chloride ($CaCl_2$, 11 mM), PI (0.25 wt%), and freeze dried GelMA (5 wt%). All components were dissolved in 40% HBSS and 60% astrocyte complete media (DMEM + 10% FBS + 1% P/S) followed by incubation at 37 °C for 1 h.

2.5. Bioink preparation

The bioink was prepared using 4 wt% GelMA, 1 wt% gelatin, 0.5 wt% alginate, and 0.25% PI dissolved in 40% HBSS, 60% MEM and incubated at 80 °C for 50 min. Next, the ink was incubated at 37 °C for 30 min. Then, NE-4Cs were dissociated and mixed with the bioink supplemented with 10 μg ml^{-1} laminin at a concentration of 25×10^6 cells ml^{-1}.

2.6. Embedded bioprinting of neural-laden ink in astrocyte-laden bath

Polydimethylsiloxane (PDMS) molds were sterilized in 70% ethanol and UV overnight, followed by a thorough washing step with sterile DPBS. The supporting astrocyte-laden bath was pipetted into the molds and kept at 4 °C for 5–8 min prior to printing. The bioink was loaded into 1 ml syringes (BD) capped with 30 G needles (blunt, BD) and mounted on the extruder of a Cellink Inkredible bioprinter. The tip of the needle was positioned at a designated point with respect to the position of the mold containing the supporting hydrogel, which represented the XYZ origin for all the printing configurations. A syringe pump (New Era Pump Systems) was used to extrude the bioink at 3 μl min^{-1}. After printing, the full structures were crosslinked under UV light (800 mW, 60 s) using an OmniCure S2000 machine. Next, the constructs were extracted from the molds, washed with DPBS and transferred to a well plate containing fresh MEM complete media (MEM + 10% FBS + 1% P/S). All printed constructs were incubated at 37 °C in 5% CO_2 in well plates immediately after crosslinking. Culture medium was changed the day after printing, and every 2 d after that until analysis was done at different time points.

2.7. Mechanical and rheological characterization

The compressive moduli of 5% GelMA hydrogels were tested (Instron 5542 instrument) at 20% strain min^{-1}. The slope of the linear region (0%–5% strain) was used to calculate compressive modulus. For rheology experiments, a linear ramp shear rate (1–100 s^{-1}) was exerted on the material and the response of the material was measured over a continuous flow. Oscillatory stress sweeps were applied over 10%–100% strain at 10 Hz to measure the response of the material to growing strain. Oscillatory time sweeps at a frequency of 10 Hz were conducted with alternating high and low strains of 250%–1% every 2 mins to measure the recovery capabilities of the bath and bioink in the presence and absence of shear for printability purposes.

2.8. Viability and metabolic activity assays

Cell viability of the cell-laden constructs was assessed using Live/Dead assay (Invitrogen) and cells were imaged with an inverted fluorescence microscope (Zeiss Axio Observer D1 Fluorescence Microscope, Carl Zeiss, Germany). The cellular metabolic activity throughout the culture lifespan was assessed using Presto Blue Reagent (Life Technologies). After 2 h of incubation at 37 °C, the reagent was collected and the absorbance was measured using a microplate reader (BioTek Synergy 2, Vermont, USA), normalizing the extracted values to the 600 nm reference wavelength. Metabolic activity was monitored on days 1, 3, 7, and 14.

2.9. Immunostaining and confocal imaging

Immunocytochemical characterization was performed by fixing the cultured cells in the structures in 4% paraformaldehyde (PFA, Electron Microscopy Sciences) and in DPBS for 20 min, treating them with 0.1% Triton-X 100 for 10 min, and washing with DPBS 3 times. The constructs were further blocked using 10% goat serum (dissolved in DPBS) for 1 h at 25 °C. After fixing, cells were introduced to primary antibodies (prepared in 10% goat serum in DPBS) overnight at 4 °C. The primary antibodies used were mouse anti-beta-III tubulin monoclonal antibody (anti-β III tubulin, 1:500, Abcam) and rabbit anti-glial fibrillary acidic protein monoclonal antibody (anti-GFAP, 1:1000, Abcam). Conjugated secondary antibodies (goat anti-mouse IgG, Invitrogen Alexa Fluor 488, and goat anti-rabbit IgG, Invitrogen Alexa Fluor 594, Thermo Fisher, 1:200) and DAPI counterstaining were used for visualization. For F-actin staining, constructs were incubated in Alexa Fluor 488 actin conjugate (Invitrogen, 1:40) for 2 h at room temperature. Fluorescence microscopy (Zeiss Axio Observer D1) and confocal microscopy (SP7, Leica) were used for imaging. Z-stack confocal imaging was performed on a Zeiss LSM 880 airyscan microscope. All images were analyzed using Fiji and ImageJ softwares.

2.10. Glutamate assay and transmitter release analysis

Glutamate assay was performed using a glutamate assay kit (Sigma Aldrich). Briefly, the constructs were incubated in the assay reaction mix for 30 min. The background and controls were prepared using non-cellular constructs. Next, the constructs were crushed using a pipette followed by centrifugation at 300 g. The supernatant was collected and analyzed by measuring the absorbance at 450 nm using a plate reader (Infinite 200 pro, Tecan Austria GmbH).

2.11. Statistical analysis

Statistical analyses were performed using Graphpad Prism software. The data was evaluated using non-parametric Kruskal–Wallis test followed by post hoc test (Dunn's test) with $p < 0.05$ considered significant.

3. Results and discussion

3.1. Fabrication of a brain-like co-culture construct with 3D cell-cell interaction

The goal of current research is to mimic the mechanical, micro-anisotropic, and spatially diverse properties of the brain via bioprinting a co-culture brain-like microstructure (figure

1). The structure between neural stem cells and their neighboring cells (e.g. neuroblasts or glial cells) regulate various functions in the brain [3]. In the adult mammalian brain, endogenous neural stem cells reside at the subventricular zone (SVZ), in the lateral ventricles, and at the subgranular zone (SGZ), in the hippocampus (figure 1(a)). Astrocytes (shown in green in figure 1(a)) are another type of neural cell that makes up the neural tissue architecture across the SVZ niches [30]. The presence of astrocytes contributes to the activation and neurogenesis of endogenous neural stem cells and leads to the generation of neuroblasts upon tissue injury [2, 31]. Following this procedure, the generated neuroblasts migrate into the lateral ventricle or down to the rostral migratory system and further differentiate into neurons [30]. As such, this mechanism directs the migration of endogenous neural stem cells into brain tissue regeneration and could be modeled to understand the mechanisms underlying neural tissue regeneration and development. As a result, *in vitro* modeling and the understanding of neural stem cell behavior rely heavily on the careful study and analysis of such neural stem cell-astrocyte interactions [32].

In the present study, two major brain cell types (i.e. neural stem cell-derived mouse neurons and mouse cortical astrocytes) were picked to create a proof-of-concept of this model by fabricating neural cell-laden channels in an astrocyte-laden matrix. The first of our aims is to mimic the anisotropic arrangement of neural stem cells and astrocytes (figure 1(a)) in the SVZ in the brain through the embedded 3D bioprinting of a neuron-laden bioink, which is composed of GelMA, gelatin, alginate, and laminin mixture (GGA bioink) (figure 1(b)). As shown in our previous studies, by applying 3D embedded bioprinting and by tuning the mechanical properties of the ink, we can create self-organizing cell-laden printed micro-fibrous structures, in which cells can migrate along to create well-aligned structures [33–35].

The astrocyte-laden GelMA matrix with its relatively low Young's modulus is designed to mimic the natural stiffness of the non-neuronal brain tissue, thus enabling *in vitro* growth and the extension of astrocytes [36]. In addition, the astrocyte-laden GelMA matrix acts as a supporting bath, which allows for the fabrication of complex 3D geometries and aligned bioprinted fibers (figure 1(b)). During the bioprinting process, the calcium ions in the GelMA supporting bath interact with the α-(14)-linked chain configuration (i.e. egg-box structure) in the alginate chains of the bioink, forming a physical crosslinking tool to fixate the printed fibers [37]. The printing process of the GGA bioink is then followed by crosslinking the astrocyte-laden GelMA matrix via ultraviolet (UV) light treatment. The variation in Young's modulus between the printed fibers and the support bath ensures that the neuronal cells are constrained to grow along and inside the bioprinted fibers (figure 1(b)). Thus, a brain-like micro-structure with constrained patterns of neural fibrous routes surrounded by an astrocyte matrix can be built to create multicellular self-organizing spheroid cultures useful for studying neuron-astrocyte interactions (figure 1(c)). This method could be further customized to enable the fabrication of patterned multi-cultures composed of self-organizing spheroids originating from diverse neuronal populations. Furthermore, inter-neuronal interactions within the spheroids and communication with glial cells could be facilitated through the current embedded bioprinting method (figure 1(c)). The fabrication process of the embedded bioprinted brain-like microstructure is

depicted in detail in the schematic design illustrated in figure S1 (available online at https://stacks.iop.org/BF/13/015014/mmedia).

3.2. Tunable physical properties of the support bath

Multi-material multi-cellular 3D geometries can be achieved with embedded bioprinting and GelMA-based biomaterials. These materials have two key physical properties which can accelerate the fabrication process: reversible thermally responsive physical gelation and photo-crosslinkability. At temperatures below 30 °C, the polymeric networks within GelMA generate a favorable stiffness to physically constrain and maintain the bioink in a fiber form at a desired position [38]. To create a support bath for embedded structures, several parameters such as the concentration and ratio of the biomaterial ingredients, rheological and mechanical properties, UV crosslinking parameters, and the degradation behavior of the crosslinked hydrogel were studied and optimized (figures 2(a)–(d)).

In embedded bioprinting, the movement of the needle inside the support bath may induce shear stress and create cracks inside the hydrogel. Achieving rapid gel recovery with no remnant cracks in the crosslinked printed structure is contingent upon the shear-thinning and thermal-healing properties of the bath. GelMA hydrogels are well suited for this purpose with their viscoelastic properties structured by the internal electrostatic hydrophobic forces and hydrogen bonding (figure 2(a) (i)) [39]. Upon insertion of the needle into the GelMA bath, some of the electrostatic and hydrogen bonds disentangle due to the shear stress imposed by the needle movement (figure 2(a) (ii)). This behavior creates aligned polymer chains and thus lower viscosities while printing (i.e. shear-thinning behavior). After the needle (i.e. shear stress) is removed, the physical bonds are formed again, and the GelMA prepolymer chains return to their original randomly oriented configuration, a property called thermal-healing behavior. A previous study also reported that the presence of calcium ions (Ca^{2+}) generated an electrostatic interaction with gelatin hydrogels, affecting the viscoelastic properties of the material [40]. Here, to enhance the shear thinning and thermal-healing behavior of the GelMA support bath, we have supplemented the pre-polymer bath solution with Ca^{2+} ions through 11 mM calcium chloride [15]. Through this addition, the interaction of Ca^{2+} with the carboxyl groups within the GelMA polymer chains becomes highly directional and the viscoelasticity is increased [40, 41]. In addition, the dispersed Ca^{2+} ions partially crosslink the alginate networks in the GGA bioink, leading to the formation of well-defined extruded microfibers with crosslinked boundaries (figure S1).

By increasing the GelMA concentration, the molecular-level physical interactions and eventually hydrogel viscosity are increased significantly (figures 2(b) and (c)). However, our studies show that the impact of Ca^{2+} on GelMA bath viscosity is substantial only at GelMA concentrations below 3 wt% (figure 2(b)). We observed no significant change in GelMA viscosity when Ca^{2+} was added to baths with GelMA concentrations above 3 wt%. Prior studies have shown that, at low GelMA concentrations, Ca^{2+} selectively formed a complex with the carboxyl groups on the GelMA backbone (i.e. $–COO^{–}–Ca^{2+}–COO^{–}–$ bond), creating an interconnected network by linking neighboring GelMA chains. This event largely impacted the viscosity. At high GelMA concentrations, on the other hand, the effects of secondary forces, such as hydrogen bonding and hydrophobic interactions [42] among the

GelMA chains were stronger than those imposed by Ca^{2+}. As such, the viscosity was not impacted substantially by the presence of Ca^{2+} [40]. This observation could be favored in embedded bioprinting where the movement of the needle within the 5% GelMA bath could be supported by the shear-thinning and thermal-healing behavior of the bath.

To confirm the thermal-healing behavior of the GelMA bath, the strain-induced damage and healing of the 5 wt% GelMA baths with Ca^{2+} were evaluated through a continuous oscillatory strain sweep (between 250% and 1% strain and at 10 Hz) [43]. 250% strain was applied for 2 min to disaggregate the structure of the hydrogel. The hydrogel was left to recover by decreasing the strain to 1% for another 2 mins. Under high dynamic strain (250%) (figure 2(d)), the storage modulus value (G') of the GelMA hydrogel was decreased to a value lower than the loss modulus (G''), and the hydrogel showed gel-to-sol transition behavior. In contrast, when the strain moved down to 1%, the storage modulus of the GelMA returned to its initial value, showing the occurrence of a rapid sol-to-gel transition. This result indicates that the GelMA bath possesses a thermal-healing behavior.

Using photo-crosslinkable hydrogels to fabricate engineered hydrogel constructs provides a relatively fast and convenient approach to create structures with high shape fidelity while having the least degree of degradation. Our previous studies demonstrated that low concentrations of GelMA hydrogels (<5 wt%) met the requirements for fabricating soft tissues with a compressive modulus of less than ~2 kPa [44], as well as proving effective in encapsulating various types of cells with sufficient cellular behavior [45]. However, forming a hydrogel from low concentrations of GelMA pre-polymer solutions is often difficult. On the other hand, GelMA concentrations of over 5 wt% compose relatively stiff hydrogels that can embed cells with a higher stiffness tolerance, such as muscle cells [34, 45]. Additionally, at higher concentrations of the GelMA pre-polymer solution (>5 wt%), physical crosslinking occurs at room temperature within a few minutes [46]. As observed in our previous studies [34], this fast physical crosslinking behavior along with the high stiffness (~3.5 kPa recorded for 7 wt% and ~11 kPa for 15 wt%GelMA) induces several large cracks during the movement of the bioprinting nozzle in the supporting gel. Moreover, the embedded bioprinting process could easily be interrupted inside stiffer GelMA hydrogels, leaving non-continuous segments in the bath. As such, to bioprint an embedded structure with brain-like stiffness, 5 wt% GelMA pre-polymer solution serves as a good candidate for a supporting bath by fulfilling both criteria: reaching brain stiffness and embedded printability.

Furthermore, the intensity level of UV treatment is often restrained by the limitations imposed by the biotic environment when a cell-laden hydrogel is being printed. It is important to maintain high cell viability by optimizing the UV exposure during the fabrication of cell-laden GelMA hydrogels. To find out the optimal UV exposure conditions, we examined a range of GelMA solution concentrations (2.0%–5.0%, w/v) and UV exposure durations (60–240 s) in fabricating GelMA constructs using a fixed concentration of the photo-initiator (0.25%, w/v) at an intensity of 800 mW. In our previous study, the optimal UV exposure time was 30 s [34]. Here, however, the thickness of the polydimethylsiloxane (PDMS) mold (i.e. the resulting brain-like structure) was 5 mm. Experimentally, such a thick structure would require twice the exposure time to be fully

crosslinked. Therefore, two 30 s UV treatment sessions were applied from the top and bottom faces of the structure, totaling 60 s of UV exposure. As demonstrated in figures 2(e) and S2(a), the chemical GelMA hydrogels were found to be fully crosslinked upon 60 s of UV treatment when the concentration of the GelMA solution was higher than 3% (w/v). It can be hypothesized that the polymer chains in low concentrations of GelMA solution provide a low crosslinking density, which is reflected in the formation of poorly crosslinked constructs [47]. Figure 2(f) shows the final crosslinked printed cell-laden construct. The embedding mold shape can be modified to fit the desired custom model geometry.

A point to consider in embedded bioprinting is the formation of microcracks inside the bath after the needle sweep during the printing process. These cracks are often larger than the GelMA pore size and could lead to unconfined cell growth, undesired changes in structure's stiffness and compromised shape quality. As such, the thermal-healing capability of the GelMA bath becomes more prominent during 3D printing, when the physical movement of the nozzle inside the bath could leave cracks behind in the crosslinked bath. Although the majority of these cracks disappear immediately during nozzle movement, microcracks can still be present in the crosslinked hydrogel [15]. The reversible transition from fluid-like to gel-like states induces the thermal-healing capability in the GelMA bath to restore its uniform structure throughout the printing process and upon crack formation (figure 2(g)). As such, we increased the temperature to 37 °C for 10 min to remove these cracks without interfering with or disturbing the 3D fibers printed inside the embedded structure. To confirm this healing behavior, we performed Scanning Electron Microscopy (SEM) imaging on the samples in three stages (figure 2(h)). First, the porous structure of the GelMA hydrogel was imaged by SEM prior to the printing process (figure 2(h) (i)). Next, the bioink was printed inside the bath at room temperature, and the crosslinked construct was imaged through SEM to confirm the formation of cracks in the bath (figure 2(h) (ii)). Upon incubating the printed and crosslinked construct at 37 °C, the SEM images confirmed that the cracks were healed to a great extent (figure 2(h) (iii)). Consequently, with their shear-thinning and thermal-healing properties, 5 wt% GelMA hydrogels can satisfy the rheological requisites of a support bath for embedded printing. Moreover, the macro or micro-sized cracks could affect the structural fidelity of the desired construct, resulting in the creation of non-continuous printed fibers in the supporting bath. To avoid the micro-sized cracks affecting the structural fidelity of the designed constructs, Ca^{2+} ions were added into the supporting gel to induce immediate physical crosslinking of the alginate in the bioink, which, in turn, could prevent the leakage of the bioink into the supporting bath following crack formation. Therefore, this fastphysical crosslinking could help to avoid micro-sized crack defects, so the structural fidelity of the desired constructs can be maintained before the annealing treatment of the constructs at 37 °C.

Creating a brain-like engineered construct in which neural cells can grow in a similar manner to the native brain requires a brain tissue-mimicking extracellular matrix (ECM). The compressive modulus of the native brain ranges from 0.6 to 1.2 kPa [48]. The stiffness required for the neural stem cell differentiation was previously reported to be maximally impactful in the initial stages of differentiation [49]. The compressive modulus of the 5 wt% GelMA hydrogels post UV exposure was measured to be 0.7 ± 0.1 kPa (figure 2(i)) which is highly comparable to that of the native tissue. Moreover, the effect of the UV exposure

time on the modulus was assessed. It was found that regulating the UV treatment between 60 and 80 s at an intensity of 800 mW maintained the compressive modulus in the measured range of the native brain, while increasing the exposure time to 90 s and beyond resulted in a modulus of over 1.5 kPa (figure 2(j)). The possible explanation for this behavior is that a modulus-enhanced phenomenon was observed in the 5 wt% GelMA hydrogel by increasing the UV exposure time. Specifically, similar to the formation of chemical hydrogels, the increment in modulus value could have stemmed from an increased release of free radicals and thus an increased crosslinking density due to the long duration of UV exposure [39].

Since the cell-laden constructs are maintained in biological culture conditions post fabrication, the crosslinked hydrogels must be stabilized for a physiological environment upon incubation at 37 °C. Insufficient crosslinking can lead to expedited and undesired hydrogel degradation during the incubation process before cell-laden construct maturation. The degradation behavior of crosslinked GelMA hydrogels was therefore evaluated and optimized with various UV exposure times. A slight weight loss was observed during 60, 70, and 80 s of UV treatment within 7 d of incubation (figure 2(k)). However, further incubation of the mentioned groups for another 7 d revealed no significance in the weight loss (figure 2(k)). Such an insignificant degree of dissolution or degradation can therefore be attributed to the poorly-crosslinked or un-crosslinked sections of the GelMA construct which would dissolve in the culture medium when incubated in the biophysiological environment. We performed mechanical testing on the crosslinked 5 wt% GelMA constructs prior to and after incubation at 37 °C to study the effect of gel degradation on the stiffness of the constructs (figure 2(l)). The results confirmed that the compressive modulus remained in the stiff region of the brain after 14 d of incubation, showing that the constructs could provide enough stiffness for neural cell growth and differentiation.

3.3. Optimizing printing parameters of the GGA bioink

Printing fiber-like structures and hierarchical networks in the supporting bath requires an injectable bioink capable of easy extrusion with no post-print deformation. Such injectable behavior of the bioink is defined by its rheological properties [50]. Previous studies have reported that GelMA and alginate endow neuron cells with a neurite outgrowth effect and promote neuronal differentiation from pluripotent cells [51–53]. Thus, we chose the GGA bioink (figure 3(a)) to create fibers with tunable viscosity, neuron-compatible stiffness and porosity. GelMA includes binding sites to which cells could attach [51, 52]. Through characterizing the concentration of GelMA, a suitable stiffness could be achieved for neuronal cell growth. Alginate facilitates the formation of fine fibers inside the bath through Ca^{2+} crosslinking. Gelatin was added to the ink to improve printability. After UV crosslinking and upon incubation at 37 °C, gelatin gradually dissolved, leading to a highly porous structure in the printed fibers [54]. First, the rheological properties were evaluated and optimized using composite bioinks with different GelMA concentrations in the GGA bioink (figures 3(b) and S3). Similar to the GelMA supporting bath, a declining trend occurred in the viscosity with each increment in the shear rate at a continuous flow rate, demonstrating the shear-thinning characteristics of the bioinks (figure S3(a)). Moreover, we observed a solid-like to liquid-like state transition upon performing a continuous oscillatory strain sweep under alternating high/low strains (250–1%). Within the high strain period

(250%), the G'' surpassed the G', indicating a rapid phase transition from solid to liquid at high strains (figure 3(b)). In contrast, we observed higher G' values than G'' in low strain periods, confirming that the bioink mechanically recovered and transitioned from liquid to solid state in these sections. The results confirmed that the GGA blend bioinks were endowed with shear-thinning characteristics and fluidic behaviors suitable for extrusion-based bioprinting. It is noteworthy to mention that, although the same rheological oscillatory sweeps were conducted for the bath and ink (figures 2(b), (c), 3(b) and (c)), the results were interpreted differently for each component. In terms of the bioink, the shear-thinning and gel-sol phase transformability properties represent the bioprintability of the material, while these properties in the support bath represent the capability of the support hydrogel to rapidly recover after a needle sweep without initiating cracks or distorting the extruded structure (figure 3(c)) [22].

The ink extrusion parameters, such as the printed fiber diameter, nozzle speed, and the flow rate of the bioink, regulate the diameters of the printed fibers and the quality of the printed structures [16]. We optimized the aforementioned parameters by printing the bioinks in the supporting bath. Discontinuity in the extruded fibers is a common issue in extrusion-based bioprinting and is often caused by excessive nozzle speeds or insufficient fluid pump flow rates. For instance (figure 3(d)), at a 3 μl min^{-1} flow rate, the printed fibers were not continuous when the nozzle speed exceeded 6 mm s^{-1}. In contrast, a 2 mm s^{-1} nozzle speed could yield a continuous printed fiber at the same flow rate. As such, these two factors should be simultaneously controlled to yield the desired fiber thickness. Previous studies have reported that the native nerve fiber tracts (*i.e.* association, commissural, and projection fibers) consisted of axon populations [55, 56] whose minimum diameters exceeded 200 μm [57–59]. Therefore, we tested the thickness of the extruded fibers using a 27 G (figure S4) and a 30 G needle (figures 3(d)–(f)) with inner diameters of 210 and 160 μm, respectively, under various nozzle moving speeds (mm s^{-1}) and bioink flow rates (μl min^{-1}). At any fixed nozzle speed and extrusion rate, the average diameter of the printed fibers using the 27 G needle was approximately 1.3 times higher than when the 30 G nozzle was used (table S1). Generally, the diameter of the printed fiber is associated with the nozzle speed and flow rate when the inner diameter of the nozzle is fixed. Thus, increasing the nozzle speed or decreasing the flow rate can both result in smaller fiber diameters (figures 3(d)–(e) and S4(b)–(e)). For instance, at 10 μl min^{-1}, the average diameters of the printed fibers using a 30 G needle at 2, 6 and 10 mm s^{-1} nozzle speeds were 294.0 ± 6.3, 223.0 ± 6.1 and 181.9 ± 24.0 μm, respectively. A curve (R^2 of 1) can be well-fitted to this data using the power law (figures 3(e), S4(d) and (e)) [60].

Moreover, we also found that the cross-sectional geometry of the printed fibers tends to be a circle with a 3 μl min^{-1} extrusion rate and 2 mm s^{-1} nozzle speed (figure 3(f)). Our previous studies indicated that cells can maintain high viability under low extrusion rates (<5 μl min^{-1}) during the printing process, and that a one-stroke painting spiral structure can be easily printed in the supporting gel [34]. As such, we selected this configuration for the optimized conditions to print well aligned straight fibers with circular cross-sections inside the support GelMA bath (figure 3(g)). The mechanical properties of the ink were tuned by varying the concentration of GelMA polymer in the bioink (figure 3(h)). The Young's modulus of the bioink containing 4% GelMA (~0.8 kPa) was found to best match

the stiffness of the brain (0.6–1.1 kPa), and thus was chosen as the optimized condition for mono-culture and co-culture printing conditions.

During the development of embryonic or injured adult brains, new immature inter-neuroblasts could be continuously produced from a neural stem/precursor cell niche (i.e. the subventricular zone (SVZ)) and could migrate rapidly toward their specific destinations, such as the olfactory bulb [61, 62]. To guide these immature neuroblasts, the rostral migratory system provides a special fibrous route to connect the neural stem/precursor cell niche and the local regions, where the neuroblasts could mature into neurons and integrate into the neuronal circuitry [63]. To evaluate the capability of our microfabrication platform in printing complex structures, such as those present in the rostral migratory system, we captured a small section of this route and printed structures with numerous branches (figure 3(i)). For instance, a large, yet simple six branch structure (radius ≈ 1 cm) with 60° angles between the adjacent branches was fabricated through the developed bioprinting method (figure 3(j) (i)) and could be further extended to form spatially complex structures with different fiber orientations and cross-branches (figures 3(j) (ii) and (iii)). The pattern from the top view resembled a crosslet (figure 3(j) (ii) inset). Moreover, to confirm the printability of the rostral migratory system architecture, which is formed through the assembly of various bifurcated structures [64], we 3D printed structures with high branch density (*e.g.* 12 branches) with 30° angles between the branches (figure 3(j) (iii)). We also bioprinted a branch-like structure similar to the rostral migratory system using an NIH3T3 cell-laden bioink, which exhibited high cell viability (figure S5). In conclusion, the remarkable printability of multi-branched spatial structures confirmed that the developed method is capable of recapitulating rostral migratory route-like structures with geometrical integrity and relatively high precision.

3.4. Successful neuronal differentiation in the 3D printed co-culture constructs

Neural stem cells and glial cells compose the major cell types in the niche at SVZ [65]. Astrocytes, a key category of glial cells, have been confirmed for their functionality in activating neural stem/precursor cells and neuroblasts, and for playing a key role in the survival of neural cells in the brain [66]. Additionally, astrocytes surrounding the rostral migratory system could form a supporting matrix and play a vital role as a meshwork-like narrow glial tunnel to guide the immature neural stem/precursor cells and neuroblasts to aggregate and form a chain-like structure; then these neural stem/precursor cells and neuroblasts could migrate through rostral migratory system to their destination [61]. To create a co-culture brain-like neurospheroid niche model, we used a neural stem cell line (NE-4C) and primary astrocytes—a major type of glial cell in the brain [67]. To build neural stem cell-laden fibers in the brain-like construct, we encapsulated NE-4Cs in the GGA bioink and printed parallel structures inside the bath using embedded bioprinting (figures 1(b) and 4(a)).

We followed a previous *in vitro* protocol to differentiate neural stem cells into neurons (figure S6) [27], and further optimized this protocol for differentiation in 3D hydrogels (figure 4). RA was shown to induce neuronal differentiation in NE-4C subcultures [27]. After adding RA, neural stem cells underwent morphological changes, aggregation and

colony formation, and started to show neuronal characteristics within 12 d and in five stages (figure 4(c)). Here, the neuron differentiation in the 3D printed neural cell-laden structures followed a similar trajectory to neuron formation through neurospheroid aggregations after adding RA to the culture media (figures 4(a) and (b)). As the efficiency of differentiation is highly dependent on the cell density after RA induction [68], it is critical to optimize the cell density at the encapsulation stage to maintain a viable concentration of neural stem cells after printing. Embedding stem cells in GGA bioinks at a concentration of 25 million ml^{-1} was found to be optimal for differentiation in 3D. Prior to adding RA to the constructs, the 3D printed constructs were cultured for 2 d *in vitro* to recover from a possible loss of cell viability as well as to allow neural stem cells to proliferate further inside the channels. As shown in figures 4(c) and (e), the increased metabolic activity of the neural cells after 5 or 7 d could have been caused by the degradation of the GelMA supporting gel (figure 2(k)), which could have contributed to enhancing the nutrient and oxygen diffusion from the medium into the 3D printed constructs. Therefore, a significant increase was observed in the metabolic activity of the neural cell-laden constructs from day 7 to day 14 (figure 4(c)), suggesting that the ink is capable of neural cell growth support.

During the initial stages of differentiation (days 3–5), the neural stem cells inside the channels transformed into loose aggregated spheroids, a condition that was also observed in 2D. After proper surface functionalization (e.g. PDL) in 2D cultures, such structures began to settle at the bottom of the well plate and spread neurites (figure S6(iv)). It was shown that by adding an ECM protein, laminin, to 3D gels, neuronal differentiation and neurite formation could be promoted [69]. As such, we added laminin to promote attachment and connections between neurospheroids. Reaching day 10 of differentiation, neuron structures started to form neuronal networks with bundled axonal bodies. In 3D gels, however, this process was further prolonged due to the varying stiffness of the hydrogel ECM. In fact, the extension of the neurites inside a 3D matrix is critically dependent on the mechanical properties of the surrounding ECM [70]. Nonetheless, from day 7 onward, the 3D printed neural cells showed an increased expression of βIII tubulin (TUJ1), a marker specific to post-mitotic neurons (figures 4(f)–(h)). Following day 14, spheroids covered the neuronal fibers (figure 4(h)), and, in some sections of the printed fibers, the neurons started to gradually sprout out from the spheroid morphologies, potentially leading to the formation of cross connections between spheroids. We hypothesized that the spreading of neurons inside the bioink was enhanced through gradual degradation of the bioink in culture, during which the K^+ ions in the culture medium gradually replaced the chelated Ca^{2+} ions in the egg-box structure of the alginate chains of the GGA bioink, resulting in the degradation of these crosslinked chains and thus the degradation of the bioink [71].

3.5 GelMA bath provides a favorable platform for glia proliferation and spreading

Next, we created a glia-mimetic gel by encapsulating astrocytes in a GelMA pre-polymer bath solution (figure 5(a)) followed by embedded printing and UV crosslinking. In order to proliferate, elongate and form networks after incubation (figure 5(b)), astrocytes require a proper ECM and anchoring substrate [72]. To optimize the ECM-like properties of the bath, astrocytes were prepared in different GelMA bath concentrations (3.5%, 5%, 7%), and were crosslinked at a UV intensity of 800 mW and at various UV exposure times (50 s, 60 s, and

80 s). As shown in figures S7 and S8, astrocytes showed good extension and migration in a 5 wt% GelMA bath and lower UV crosslinking durations (*i.e.* 50 s and 60 s). To further assess the viability of astrocytes with various UV crosslinking times, a live and dead assay was performed on the constructs after UV crosslinking (figures 5(c) and S8). As shown in figure 5(c), astrocytes showed high viability (>80%) at 800 mW of UV power and under 100 s of UV exposure. The loss of cell viability could pertain to the stress imposed during the encapsulation, free radicals generated by the photo-initiator, or long UV exposure times. At prolonged UV exposure times (>100 s), a significant loss of viability was observed, probably due to the damage caused by a surplus of free radicals [73]. As a result, 60 s is the suggested UV crosslinking duration to create a suitable culture environment for the encapsulated astrocytes. This observation was further confirmed by the increase in astrocyte metabolic activity 14 d after culture *in vitro* (figure 5(d)).

3.6. A viable microenvironment for bioprinted neurospheroid and glial hybrids

Next, we fabricated a brain-like co-culture construct with embedded printing using the neural stem cell-laden bioink in the astrocyte-laden bath figure 5(e)). After 7 d of incubation, neural cells showed good spreading morphology in the printed nerve fibers (figure 5(f) (i)). By keeping the neural stem cells in the culture until day 14, confluent fibers could be observed with elongated morphologies, suggesting that the ECM properties of the bioink were suitable for neural stem cell growth and spreading (figure 5(f) (ii)). In various sections of the bath, astrocytes also formed elongated interconnected networks over the course of 14 d. Encapsulated astrocytes were labeled with an astrocyte specific marker (GFAP) to study cell morphology and network formation in the bath (figures 5(g) (i)–(ii)). Confocal imaging and 3D reconstruction of the immunostained constructs on day 7 (figure 5(g) (iii)) revealed that most astrocytes still maintained a round morphology with the exception of only a few cells interconnected and extended into a spindle morphology. On day 14, on the other hand, a large network of astrocytes was observed due to the gradual degradation of the bath (figure 5(g) (iv)), providing the astrocytes with spatial vacancies to grow and spread throughout the bath. By inducing differentiation in the co-culture constructs, interconnected networks were formed within the spheroids within 14 d of culture, leading to the formation of a patterned self-organizing brain-like structure with astrocytes surrounding the spheroid channels (figures 5(h) (i)–(iii)). One of the main considerations in co-culture tissue models is to optimize a common culture medium for the different cell types. Effective differentiation of neural stem cells into neuronal subtypes requires a serum-free conditioned media, while the glial culture relies on serum-containing media for proliferation. Studies which target neuron-glia co-culture models have used different methods for media supplements. For instance, Aregueta-Robles *et al* mediated the co-culture media by using a 1:1 composition of the media specific to each cell type [74]. Other studies showed that astrocytes can survive and be cultured in the neuron-maintaining medium [75, 76]. We performed a study to optimize the common co-culture media compositions for both neuron differentiation and astrocyte growth (figure S9). Astrocytes were cultured in various neuron-supportive media including neurobasal medium supplemented with B27 (NBM), and defined medium (DM, serum free media including ITS) as recommended by previous research [77]. For control groups, we chose astrocyte media (DMEM, 10% FBS) and neural stem cell media (MEM, l% FBS). After 7 d of culture, astrocytes showed good survival in the DM medium as

opposed to the NBM group. High expression of the GFAP marker confirmed the survival and preservation of astrocyte phenotypes in the DM media. As a result, DM was chosen as the common media for maintaining all co-culture constructs. Notably, as reported in our previous study, the astrocyte differentiation of neural stem cells is enhanced once the culture medium is supplemented with serum [78]. However, high TUJ1 expression of cells at the printed niche in the co-culture system with serum indicates that astrocytes may promote the neuronal differentiation of neural stem cells, similar to the case observed here [2]. Furthermore, in regions near the interface of the spheroid channels and the astrocyte bath, we observed that astrocytes maintained a less spindled morphology and showed a tendency towards a more rounded morphology (figure 5(i) (ii)). In sparse areas of the bath where neurons/neuronal progenitor cells had migrated into the astrocyte bath, we observed that the neural cells expressed TUJ1, but maintained a round morphology without extending neurites (figure 5(i) (iii)). This formation could be explained by the higher mechanical properties of the bath compared to the ink material (figures 2(i) and 3(h)) and suggests that the formation of neurospheroids is contingent on the fine-tuning of the material stiffness. We tested various compositions of the GGA bioink by adjusting the concentration of alginate (figure S10). As shown in figure S10(a), neurospheroids in inks containing alginate 0.1% and alginate 0.2% were smaller in size and gradually tended to interconnect with their neighboring spheroids. Neural cells in the ink with 0.5% alginate, on the other hand, self-organized into larger and more discrete neurospheroids. Finally, as a proof of concept, we also measured the amount of glutamate produced in the co-culture system (figure S11). It is well known that neurons in the central nervous system can release and transport neurotransmitters such as glutamate to regulate physiological functions; however, excess glutamate release from the neurons results in the overstimulation and destruction of neural cells, a phenomenon called excitotoxicity [18]. Averting this condition, astrocytes uptake and recycle the excess levels of glutamate into glutamine. The translated glutamine can be released from the astrocytes and reabsorbed by the neurons. This process is known as the glutamate-glutamine cycle (figures S11(i) and (ii)) [19]. Using this mechanism, the glutamate concentration can remain in equilibrium in the brain. As shown in figure S11(iii), the neuron mono-culture showed higher amounts of released glutamate compared to the co-culture and astrocyte mono-culture. Notably, compared with the neuron mono-culture group, the concentration of glutamate in the co-culture group experienced a reduction in the presence of astrocytes in the brain-like construct. This difference may be attributed to the role of adjacent astrocytes in the uptake of the glutamate produced by the neurons in the printed fibers and the bath. Finally, we concluded that this variation in size and connectivity was mainly caused by the variation in stiffness (tuned through alginate concentration) in the three bioinks. As a result, the mechanical properties of the ink could be optimized in various ways (e.g. altering the bioink concentration, UV exposure time, or chemical crosslinking ratio) such that the desired geometry and connectivity of the neurospheroids could be achieved. By adjusting the stiffness of the ink and bath biomaterials, the developed brain-like co-culture construct could effectively interface neurospheorids with glial populations and thus could provide a pathway towards modeling the 3D neural stem cell niche.

The use of the proposed additive manufacturing techniques, and the selection and engineering of smart biomaterials could considerably push organoid- and spheroid-based

research towards a streamlined and reproducible platform where the fabrication of these structures could be conveniently scaled up to allow for high throughput analyses. By building a diverse bank of organoids and spheroids based on reprogrammed induced pluripotent stem cell (iPSC) lines, we could ultimately combine this technology with automated multi-material printing systems for the rapid manufacturing of complex amalgamated microarchitectures for organ-organ interactions using the organoid building blocks [79]. These platforms could serve as major stepping stones towards modeling the stem cell niche in the brain, which has not yet been fully established. On the other hand, since the development of the human brain requires a relatively longer time than that of a rodent, these organoids need to be cultured for months before serving as a stage-matched disease modeling platform. Consequently, modeling stem cell behavior for late-stage neurodegenerative disorders such as Alzheimer's for regeneration in an animal would require extensive experimental timelines. During this time, it would be essential to ensure the viability and functionality of the organoids and spheroids in the 3D printed neurospheroid constructs. An effective method to fortify these 3D printed cultures would be to add pre-vascularized and perfused channels within the organoids [4, 80]. Finally, the proposed 3D bioprinted platform could robustly be assimilated into an automated culture pipeline to directly manufacture, assemble, culture and test the neurospheoridand organoid-laden constructs in a scalable fashion with reduced variability.

4. Conclusion

We have optimized and characterized a brain-like co-culture construct using 3D embedded printing to fabricate neurospheroid-laden fibers inside an astrocyte-laden support hydrogel. We demonstrated that the optimized system could support the growth and differentiation of neural stem cells and astrocytes. Moreover, we showed the feasibility of fabricating free-standing complex structures by patterning self-organizing neurospheorids. The flexibility of current 3D bioprinting methods could be used to our advantage in creating diverse neuronal populations within heterogenous spheroid cultures. As such, spatial gradients of nerual stem cells could be generated by adjusting the printing parameters. Designing 3D brain co-culture models would also be more practicable as diverse neural populations could extend neurites within the printed fibers and cross-communicate, as seen in the developing or adult brain. Finally, the brain-like co-culture constructs could provide a means to study and engineer a heterogenous neural stem cell niche.

Supplementary Material

Refer to Web version on PubMed Central for supplementary material.

Acknowledgments

This paper was funded by the National Institutes of Health (R01AR074234 and R21EB026824), the Gillian Reny Stepping Strong Center for Trauma Innovation, and AHA Innovative Project Award (19IPLOI34660079). A K was partially supported by the National Institutes of Health (EB021857, AR073135, AR074234, UG3TR003148, GM126571). Y C Li was funded by the Taiwan Bio-Development Foundation, Ministry of Science and Technology, Taiwan (MOST 107-2314-B-035-001-MY2). Y Jodat would like to thank the department of Mechanical Engineering at Stevens Institute of Technology for their support in this project. R Samanipour, M Hoorfar were funded by the Natural Sciences and Engineering Research Council of Canada (NSERC) Discovery Grant.

References

[1]. Conover JC and Shook BA 2011 Aging of the subventricular zone neural stem cell niche Aging Dis. 2 49–63 [PubMed: 22396866]

[2]. Luo L, Guo K, Fan W, Lu Y, Chen L, Wang Y, Shao Y, Wu G, Xu J and Lu L 2017 Niche astrocytes promote the survival, proliferation and neuronal differentiation of co-transplanted neural stem cells following ischemic stroke in rats Exp. Ther. Med 13 645–50 [PubMed: 28352345]

[3]. Bond AM, Ming GL and Song H 2015 Adult mammalian neural stem cells and neurogenesis: five decades later Cell Stem Cell 17 385–95 [PubMed: 26431181]

[4]. Cakir B, Xiang Y, Tanaka Y, Kural MH, Parent M, Kang Y-J, Chapeton K, Patterson B, Yuan Y and He C-S 2019 Engineering of human brain organoids with a functional vascular-like system Nat. Methods 16 1–7 [PubMed: 30573832]

[5]. Heide M, Huttner WB and Mora-Bermúdez F 2018 Brain organoids as models to study human neocortex development and evolution Curr. Opin. Cell Biol 55 8–16 [PubMed: 30006054]

[6]. Brown J, Quadrato G and Arlotta P 2018 Current Topics in Developmental Biology (Amsterdam: Elsevier) 99–122

[7]. Jorfi M, D'Avanzo C, Tanzi RE, Kim DY and Irimia D 2018 Human neurospheroid arrays for in vitro studies of Alzheimer's disease Sci. Rep 8 2450 [PubMed: 29402979]

[8]. Lancaster MA, Renner M, Martin CA, Wenzel D, Bicknell LS, Hurles ME, Homfray T, Penninger JM, Jackson AP and Knoblich JA 2013 Cerebral organoids model human brain development and microcephaly Nature 501 373–9 [PubMed: 23995685]

[9]. Pasca AM et al. 2015 Functional cortical neurons and astrocytes from human pluripotent stem cells in 3D culture Nat. Methods 12 671–8 [PubMed: 26005811]

[10]. Joung D, Truong V, Neitzke CC, Guo SZ, Walsh PJ, Monat JR, Meng F, Park SH, Dutton JR and Parr AM 2018 3D printed stem-cell derived neural progenitors generate spinal cord scaffolds Adv. Funct. Mater 28 1801850 [PubMed: 32595422]

[11]. Park J, Lee BK, Jeong GS, Hyun JK, Lee CJ and Lee SH 2015 Three-dimensional brain-on-a-chip with an interstitial level of flow and its application as an in vitro model of Alzheimer's disease Lab Chip 15 141–50 [PubMed: 25317977]

[12]. Xiang Y, Tanaka Y, Patterson B, Kang Y-J, Govindaiah G, Roselaar N, Cakir B, Kim K-Y, Lombroso AP and Hwang S-M 2017 Fusion of regionally specified hPSC-derived organoids models human brain development and interneuron migration Cell Stem Cell 21 383–98. e7 [PubMed: 28757360]

[13]. Yin X, Mead BE, Safaee H, Langer R, Karp JM and Levy O 2016 Engineering stem cell organoids Cell Stem Cell 18 25–38 [PubMed: 26748754]

[14]. Highley CB, Rodell CB and Burdick JA 2015 Direct 3D printing of shear-thinning hydrogels into self-healing hydrogels Adv. Mater 27 5075–9 [PubMed: 26177925]

[15]. Hinton TJ, Jallerat Q, Palchesko RN, Park JH, Grodzicki MS, Shue HJ, Ramadan MH, Hudson AR and Feinberg AW 2015 Three-dimensional printing of complex biological structures by freeform reversible embedding of suspended hydrogels Sci. Adv 1 e1500758 [PubMed: 26601312]

[16]. Bhattacharjee T, Zehnder SM, Rowe KG, Jain S, Nixon RM, Sawyer WG and Angelini TE 2015 Writing in the granular gel medium Sci. Adv 1 e1500655 [PubMed: 26601274]

[17]. Bordoni M, Karabulut E, Kuzmenko V, Fantini V, Pansarasa O, Cereda C and Gatenholm P 2020 3D printed conductive nanocellulose scaffolds for the differentiation of human neuroblastoma cells Cells 9 682

[18]. Compaan AM, Song K and Huang Y 2019 Gellan fluid gel as a versatile support bath material for fluid extrusion bioprinting ACS Appl. Mater. Interfaces 11 5714–26 [PubMed: 30644714]

[19]. Hinton TJ, Hudson A, Pusch K, Lee A and Feinberg AW 2016 3D printing PDMS elastomer in a hydrophilic support bath via freeform reversible embedding ACS Biomater. Sci. Eng 2 1781–6 [PubMed: 27747289]

[20]. McCormack A, Highley CB, Leslie NR and Melchels FP 2020 3D printing in suspension baths: keeping the promises of bioprinting afloat Trends Biotechnol. 38 584–93 [PubMed: 31955894]

[21]. Kolesky DB, Truby RL, Gladman AS, Busbee TA, Homan KA and Lewis JA 2014 3D bioprinting of vascularized, heterogeneous cell-laden tissue constructs Adv. Mater 26 3124–30 [PubMed: 24550124]

[22]. Muth JT, Vogt DM, Truby RL, Menguc Y, Kolesky DB, Wood RJ and Lewis JA 2014 Embedded 3D printing of strain sensors within highly stretchable elastomers Adv. Mater 26 6307–12 [PubMed: 24934143]

[23]. Shirahama H, Lee BH, Tan LP and Cho NJ 2016 Precise tuning of facile one-pot gelatin methacryloyl (GelMA) synthesis Sci. Rep 6 31036 [PubMed: 27503340]

[24]. Loessner D, Meinert C, Kaemmerer E, Martine LC, Yue K, Levett PA, Klein TJ, Melchels FP, Khademhosseini A and Hutmacher DW 2016 Functionalization, preparation and use of cell-laden gelatin methacryloyl-based hydrogels as modular tissue culture platforms Nat. Protocols 11 727–46 [PubMed: 26985572]

[25]. Lee J et al. 2019 Nanoparticle-based hybrid scaffolds for deciphering the role of multimodal cues in cardiac tissue engineering ACS Nano 13 12525–39 [PubMed: 31621284]

[26]. Schildge S, Bohrer C, Beck K and Schachtrup C 2013 Isolation and culture of mouse cortical astrocytes J. Vis. Exp e50079

[27]. Varga BV, Hadinger N, Gocza E, Dulberg V, Demeter K, Madarasz E and Herberth B 2008 Generation of diverse neuronal subtypes in cloned populations of stem-like cells BMC Dev. Biol 8 89 [PubMed: 18808670]

[28]. Zhang J, Gao Y, Yu M, Wu H, Ai Z, Wu Y, Liu H, Du J, Guo Z and Zhang Y 2015 Retinoic acid induces embryonic stem cell differentiation by altering both encoding RNA and microRNA expression PloS One 10 e0132566 [PubMed: 26162091]

[29]. Orsolits B, Borsy A, Madarasz E, Meszaros Z, Kohidi T, Marko K, Jelitai M, Welker E and Kornyei Z 2013 Retinoid machinery in distinct neural stem cell populations with different retinoid responsiveness Stem Cells Dev. 22 2777–93 [PubMed: 23734950]

[30]. Liu Y, Liu RR, Wang L, Zeng L, Long ZY and Wu YM 2012 The effects of different phenotype astrocytes on neural stem cells differentiation in co-culture Neurosci. Lett 508 61–66 [PubMed: 22206833]

[31]. Li YC, Tsai LK and Young TH 2016 Intraventricular infusion of a low fraction of serum enhances neurogenesis and improves recovery in a rodent stroke model Neurosci. Lett 611 14–20 [PubMed: 26598023]

[32]. Otsuki L and Brand AH 2020 Quiescent neural stem cells for brain repair and regeneration: lessons from model systems Trends Neurosci. 43 213–26 [PubMed: 32209453]

[33]. Jia W et al. 2016 Direct 3D bioprinting of perfusable vascular constructs using a blend bioink Biomaterials 106 58–68 [PubMed: 27552316]

[34]. Zhu K et al. 2017 Gold nanocomposite bioink for printing 3D cardiac constructs Adv. Funct. Mater 27 1605352 [PubMed: 30319321]

[35]. de Melo BA, Jodat YA, Mehrotra S, Calabrese MA, Kamperman T, Mandal BB, Santana MH, Alsberg E, Leijten J and Shin SR 2019 3D printed cartilage-like tissue constructs with spatially controlled mechanical properties Adv. Funct. Mater 29 1906330 [PubMed: 34108852]

[36]. Sofroniew MV and Vinters HV 2010 Astrocytes: biology and pathology Acta Neuropathol. 119 7–35 [PubMed: 20012068]

[37]. Kühbeck D, Mayr J, Häring M, Hofmann M, Quignardb F and Díaz DD 2015 Evaluation of the nitroaldol reaction in the presence of metal ion-crosslinked alginates New J. Chem 39 2306–15

[38]. Pepelanova I, Kruppa K, Scheper T and Lavrentieva A 2018 Gelatin-methacryloyl (GelMA) hydrogels with defined degree of functionalization as a versatile toolkit for 3D cell culture and extrusion bioprinting Bioengineering 5 55

[39]. Yue K, Trujillo-de Santiago G, Alvarez MM, Tamayol A, Annabi N and Khademhosseini A 2015 Synthesis, properties, and biomedical applications of gelatin methacryloyl (GelMA) hydrogels Biomaterials 73 254–71 [PubMed: 26414409]

[40]. Chatterjee S and Bohidar HB 2005 Effect of cationic size on gelation temperature and properties of gelatin hydrogels Int. J. Biol. Macromol 35 81–88 [PubMed: 15769519]

[41]. Herning T, Djabourov M, Leblond J and Takerkart G 1991 Conformation of gelatin chains in aqueous solutions: 2. A quasi-elastic light scattering study Polymer 17 3211–7

[42]. Bergsma J, Leermakers FAM and van der Gucht J 2015 Interactions between nodes in a physical gel network of telechelic polymers; self-consistent field calculations beyond the cell model Phys. Chem. Chem. Phys 17 9001–14 [PubMed: 25751455]

[43]. Zhang Y, Tao L, Li S and Wei Y 2011 Synthesis of multiresponsive and dynamic chitosan-based hydrogels for controlled release of bioactive molecules Biomacromolecules 12 2894–901 [PubMed: 21699141]

[44]. Nichol JW, Koshy ST, Bae H, Hwang CM, Yamanlar S and Khademhosseini A 2010 Cell-laden microengineered gelatin methacrylate hydrogels Biomaterials 31 5536–44 [PubMed: 20417964]

[45]. Colosi C, Shin SR, Manoharan V, Massa S, Costantini M, Barbetta A, Dokmeci MR, Dentini M and Khademhosseini A 2016 Microfluidic bioprinting of heterogeneous 3D tissue constructs using low-viscosity bioink Adv. Mater 28 677–84 [PubMed: 26606883]

[46]. Dong Z, Yuan Q, Huang K, Xu W, Liu G and Gu Z 2019 Gelatin methacryloyl (GelMA)-based biomaterials for bone regeneration RSC Adv. 9 17737–44

[47]. Cha C, Kim SY, Cao L and Kong H 2010 Decoupled control of stiffness and permeability with a cell-encapsulating poly(ethylene glycol) dimethacrylate hydrogel Biomaterials 31 4864–71 [PubMed: 20347136]

[48]. van Dommelen JA, van der Sande TP, Hrapko M and Peters GW 2010 Mechanical properties of brain tissue by indentation: interregional variation J. Mech. Behav. Biomed. Mater 3 158–66 [PubMed: 20129415]

[49]. Rammensee S, Kang MS, Georgiou K, Kumar S and Schaffer DV 2017 Dynamics of mechanosensitive neural stem cell differentiation Stem Cells 35 497–506 [PubMed: 27573749]

[50]. Rodell CB, Mealy JE and Burdick JA 2015 Supramolecular guest-host interactions for the preparation of biomedical materials Bioconjug. Chem 26 2279–89 [PubMed: 26439898]

[51]. Wu Y, Xiang Y, Fang J, Li X, Lin Z, Dai G, Yin J, Wei P and Zhang D 2019 The influence of the stiffness of GelMA substrate on the outgrowth of PC12 cells Biosci. Rep 39

[52]. Bozza A, Coates EE, Incitti T, Ferlin KM, Messina A, Menna E, Bozzi Y, Fisher JP and Casarosa S 2014 Neural differentiation of pluripotent cells in 3D alginate-based cultures Biomaterials 35 4636–45 [PubMed: 24631250]

[53]. Kadri R, Messaoud GB, Tamayol A, Aliakbarian B, Zhang HY, Hasan M,Sánchez-Gonzáleza L and Arab-Tehrany E 2016 Preparation and characterization of nanofunctionalized alginate/methacrylated gelatin hybrid hydrogels RSC Adv. 6 27879–84

[54]. Davidenko N, Schuster CF, Bax DV, Raynal N, Farndale RW, Best SM and Cameron RE 2015 Control of crosslinking for tailoring collagen-based scaffolds stability and mechanics Acta Biomater. 25 131–42 [PubMed: 26213371]

[55]. Koutsarnakis C, Liakos F, Liouta E, Themistoklis K, Sakas D and Stranjalis G 2016 The cerebral isthmus: fiber tract anatomy, functional significance, and surgical considerations J. Neurosurg 124 450–62 [PubMed: 26361277]

[56]. Wakana S, Jiang H, Nagae-Poetscher LM, van Zijl PC and Mori S 2004 Fiber tract-based atlas of human white matter anatomy Radiology 230 77–87 [PubMed: 14645885]

[57]. Axer M, Amunts K, Grassel D, Palm C, Dammers J, Axer H, Pietrzyk U and Zilles K 2011 A novel approach to the human connectome: ultra-high resolution mapping of fiber tracts in the brain Neuroimage 54 1091–101 [PubMed: 20832489]

[58]. Chereau R, Saraceno GE, Angibaud J, Cattaert D and Nagerl UV 2017 Superresolution imaging reveals activity-dependent plasticity of axon morphology linked to changes in action potential conduction velocity Proc. Natl Acad. Sci. USA 114 1401–6 [PubMed: 28115721]

[59]. Del Toro D, Ruff T, Cederfjall E, Villalba A, Seyit-Bremer G, Borrell V and Klein R 2017 Regulation of cerebral cortex folding by controlling neuronal migration via FLRT adhesion molecules Cell 169 621–35.e16 [PubMed: 28475893]

[60]. Yeh YC, Highley CB, Ouyang L and Burdick JA 2016 3D printing of photocurable poly(glycerol sebacate) elastomers Biofabrication 8 045004 [PubMed: 27716633]

[61]. Sun W, Kim H and Moon Y 2010 Control of neuronal migration through rostral migration stream in mice Anat. Cell Biol 43 269–79 [PubMed: 21267400]

[62]. Kaneko N, Sawada M and Sawamoto K 2017 Mechanisms of neuronal migration in the adult brain J. Neurochem 141 835–47 [PubMed: 28251650]

[63]. O'Donnell JC, Katiyar KS, Panzer KV and Cullen DK 2018 A tissue-engineered rostral migratory stream for directed neuronal replacement Neural Regen. Res 13 1327–31 [PubMed: 30106034]

[64]. Alberti S et al. 2005 Neuronal migration in the murine rostral migratory stream requires serum response factor Proc. Natl Acad. Sci. USA 102 6148–53 [PubMed: 15837932]

[65]. Reynolds BA and Weiss S 1992 Generation of neurons and astrocytes from isolated cells of the adult mammalian central nervous system Science 255 1707–10 [PubMed: 1553558]

[66]. Platel JC and Bordey A 2016 The multifaceted subventricular zone astrocyte: from a metabolic and pro-neurogenic role to acting as a neural stem cell Neuroscience 323 20–28 [PubMed: 26546469]

[67]. Laywell ED, Rakic P, Kukekov VG, Holland EC and Steindler DA 2000 Identification of a multipotent astrocytic stem cell in the immature and adult mouse brain Proc. Natl Acad. Sci. USA 97 13883–8 [PubMed: 11095732]

[68]. Tárnok K, Pataki Á, Kovács J, Schlett K and Madarász E 2002 Stage-dependent effects of cell-to-cell connections on in vitro induced neurogenesis Eur. J. Cell Biol 81 403–12 [PubMed: 12160148]

[69]. Swindle-Reilly KE, Papke JB, Kutosky HP, Throm A, Hammer JA, Harkins AB and Willits RK 2012 The impact of laminin on 3D neurite extension in collagen gels J. Neural Eng 9 046007 [PubMed: 22736189]

[70]. Zhuang P, Sun AX, An J, Chua CK and Chew SYJB 2018 3D neural tissue models: from spheroids to bioprinting Biomaterials 154 113–33 [PubMed: 29120815]

[71]. Hong SH, Shin M, Lee J, Ryu JH, Lee S, Yang JW, Kim WD and Lee H 2016 STAPLE: stable alginate gel prepared by linkage exchange from ionic to covalent bonds Adv. Healthcare Mater 5 75–79

[72]. Frey L, Bandaru P, Zhang YS, O'Kelly K, Khademhosseini A and Shin SR 2017 A dual-layered microfluidic system for long-term controlled in situ delivery of multiple anti-inflammatory factors for chronic neural applications Adv. Funct. Mater 28 1702009 [PubMed: 32774196]

[73]. Shin SR et al. 2012 Carbon nanotube reinforced hybrid microgels as scaffold materials for cell encapsulation ACS Nano 6 362–72 [PubMed: 22117858]

[74]. Aregueta-Robles UA, Lim KS, Martens PJ, Lovell NH, Poole-Warren LA and Green R 2015 Producing 3D neuronal networks in hydrogels for living bionic device interfaces 2015 37th Annual Int. Conf. of the IEEE Eng. Med. Biol. Soc. pp 2600–3

[75]. Krencik R, Seo K, van Asperen JV, Basu N, Cvetkovic C, Barlas S, Chen R, Ludwig C, Wang C and Ward ME 2017 Systematic three-dimensional coculture rapidly recapitulates interactions between human neurons and astrocytes Stem Cell Rep 9 1745–53

[76]. Efremova L 2015 Development of neuron-astrocyte co-culture system for mechanistic and pharmacological studies in neurodegeneration PhD Thesis

[77]. Pozzi D, Ban J, Iseppon F and Torre V 2017 An improved method for growing neurons: comparison with standard protocols J. Neurosci. Methods 280 1–10 [PubMed: 28137433]

[78]. Li YC, Lin YC and Young TH 2012 Combination of media, biomaterials and extracellular matrix proteins to enhance the differentiation of neural stem/precursor cells into neurons Acta Biomater. 8 3035–48 [PubMed: 22548842]

[79]. Skylar-Scott MA, Uzel SG, Nam LL, Ahrens JH, Truby RL, Damaraju S and Lewis JA 2019 Biomanufacturing of organ-specific tissues with high cellular density and embedded vascular channels Sci. Adv 5 eaaw2459 [PubMed: 31523707]

[80]. Kolesky DB, Homan KA, Skylar-Scott MA and Lewis JA 2016 Three-dimensional bioprinting of thick vascularized tissues Proc. Natl Acad. Sci. USA 113 3179–84 [PubMed: 26951646]

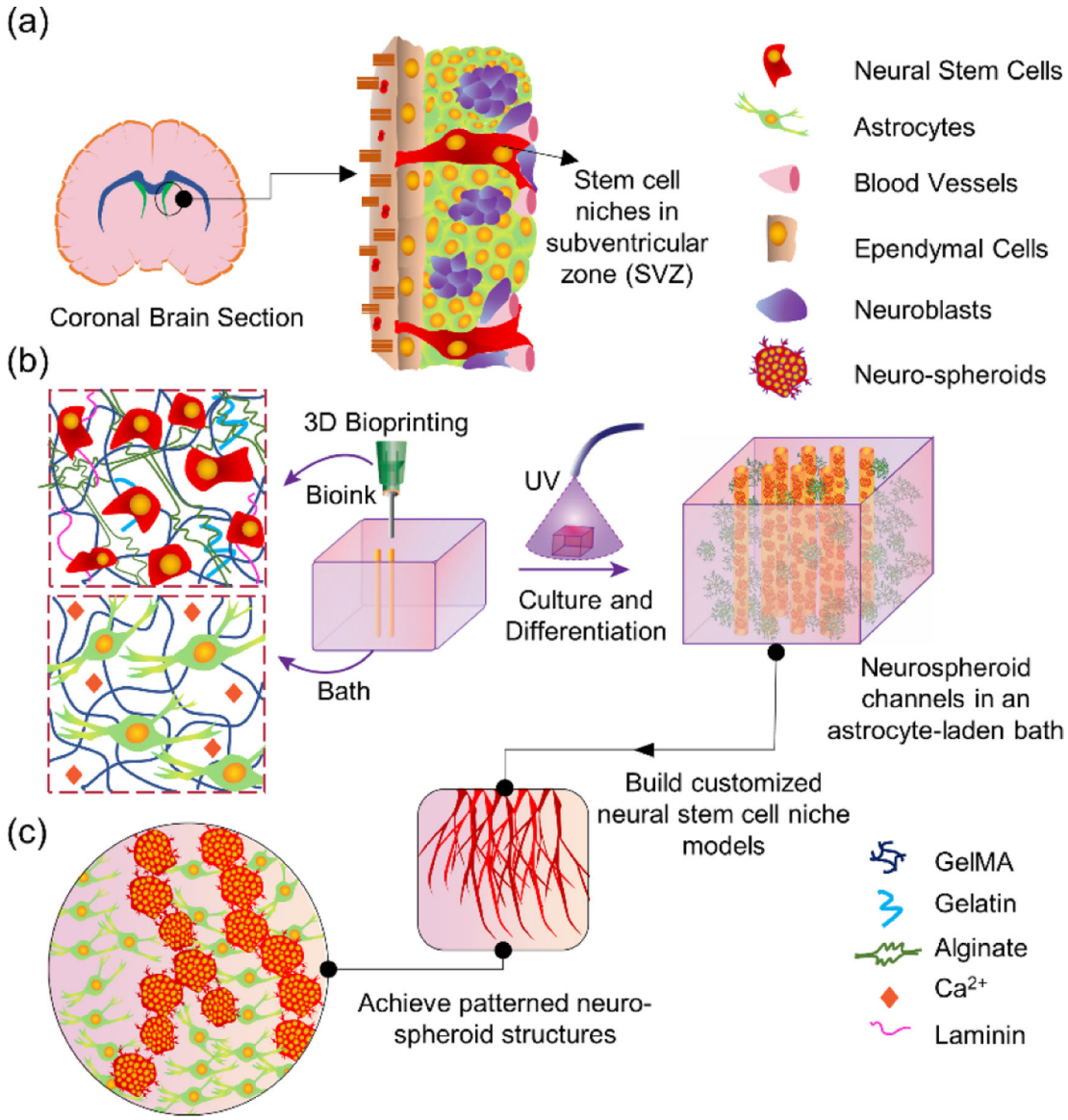

Figure 1.

(a) Schematic diagram of the coronal brain section and the stem cell niches located in the subventricular zone. Astrocytes (shown in green) and neural stem cells (shown in red) are in close vicinity and interact. (b) Schematic diagram denoting the fabrication process of 3D brain-like co-culture constructs using embedded printing. The neural cell-laden bioink is printed inside an astrocyte-laden support bath followed by UV crosslinking and *in vitro* culture. (c) Using the proposed method, it is feasible to pattern and structure various types of neurospheroid, such as excitatory and inhibitory, and glial cells to achieve 3D disease models.

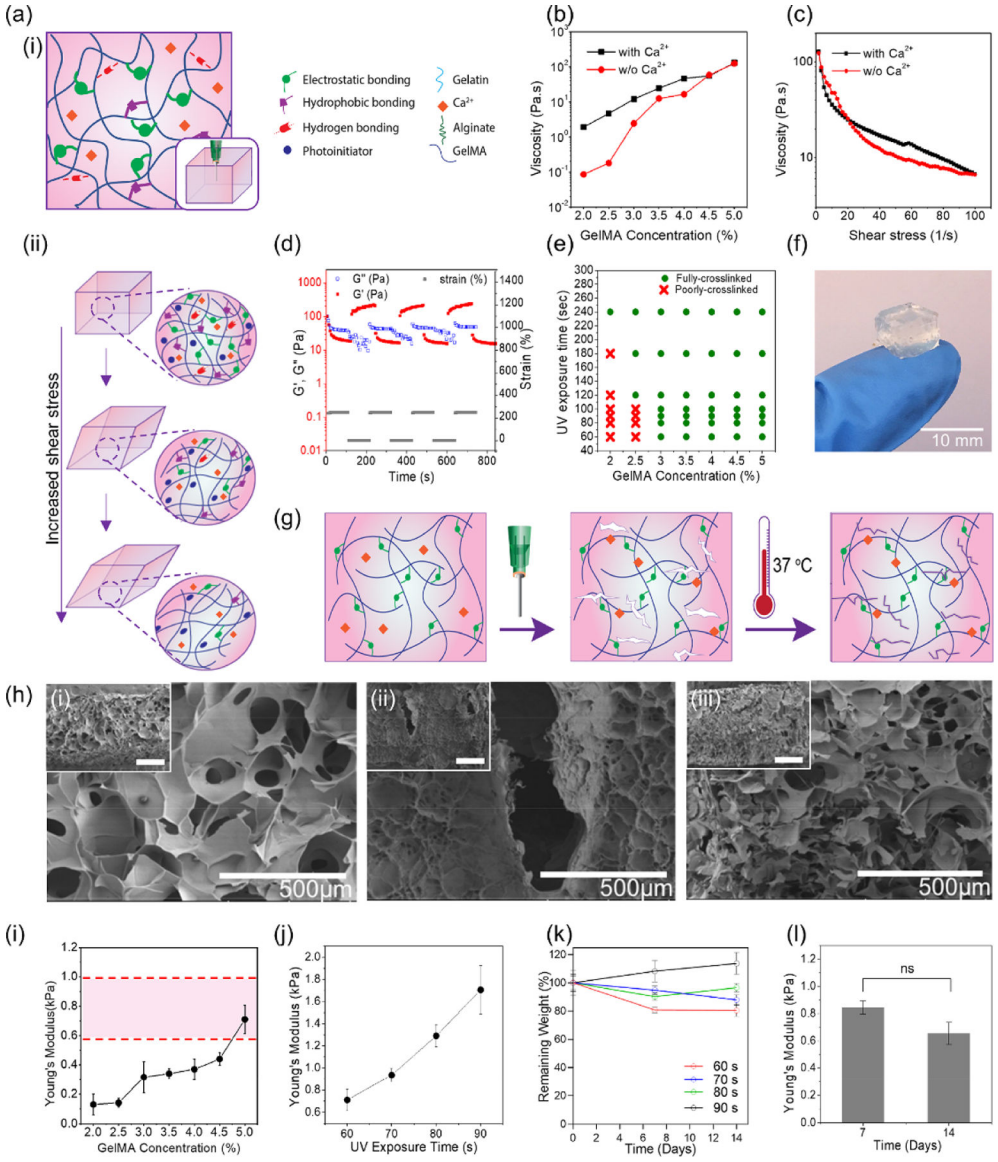

Figure 2.

Optimizing GelMA support bath. (a) Schematic process of the dynamic structure change of the GelMA solution under shear stress. (b) The effect of calcium ions on the viscosity of the GelMA solution with different concentrations ($n = 3$). (c) The effect of calcium ions on the shear-thinning behavior of 5% GelMA baths ($n = 3$). (d) Oscillatory strain sweep between low (1%) and high (250%) strain shows the rapid phase transition from gel-like to fluid-like behavior of 5% GelMA bath, necessary for the fast fix of the bioinks ($n = 3$). All bioinks were measured at 25 °C for graphs (b)–(d). (e) The effect of UV exposure time on crosslinking quality of different GelMA bath concentrations ($n = 3$). (f) Optical imaging showing macroscale morphology of the 5% GelMA bath. (g) Schematic process showing the thermal-healing behavior of GelMA baths under shear stress triggered upon needle movement. (h) SEM images of 5% GelMA bath before (left) and after (middle) the movement of the nozzle in the bath, showing the thermal-healing process (right) of

the cracks in the bath. (i) Young's modulus of different GelMA bath concentrations. UV exposure time was 60 s for all bioinks ($n = 3$). (j) The effect of UV exposure time on the stiffness (Young's modulus) of the 5% GelMA bath ($n = 3$). (k) UV exposure time affecting the degradation of 5% GelMA baths over the course of culture ($n = 3$). (l) Change in Young's modulus of the 5% GelMA bath over the two-week *in vitro* culture ($n = 3$).

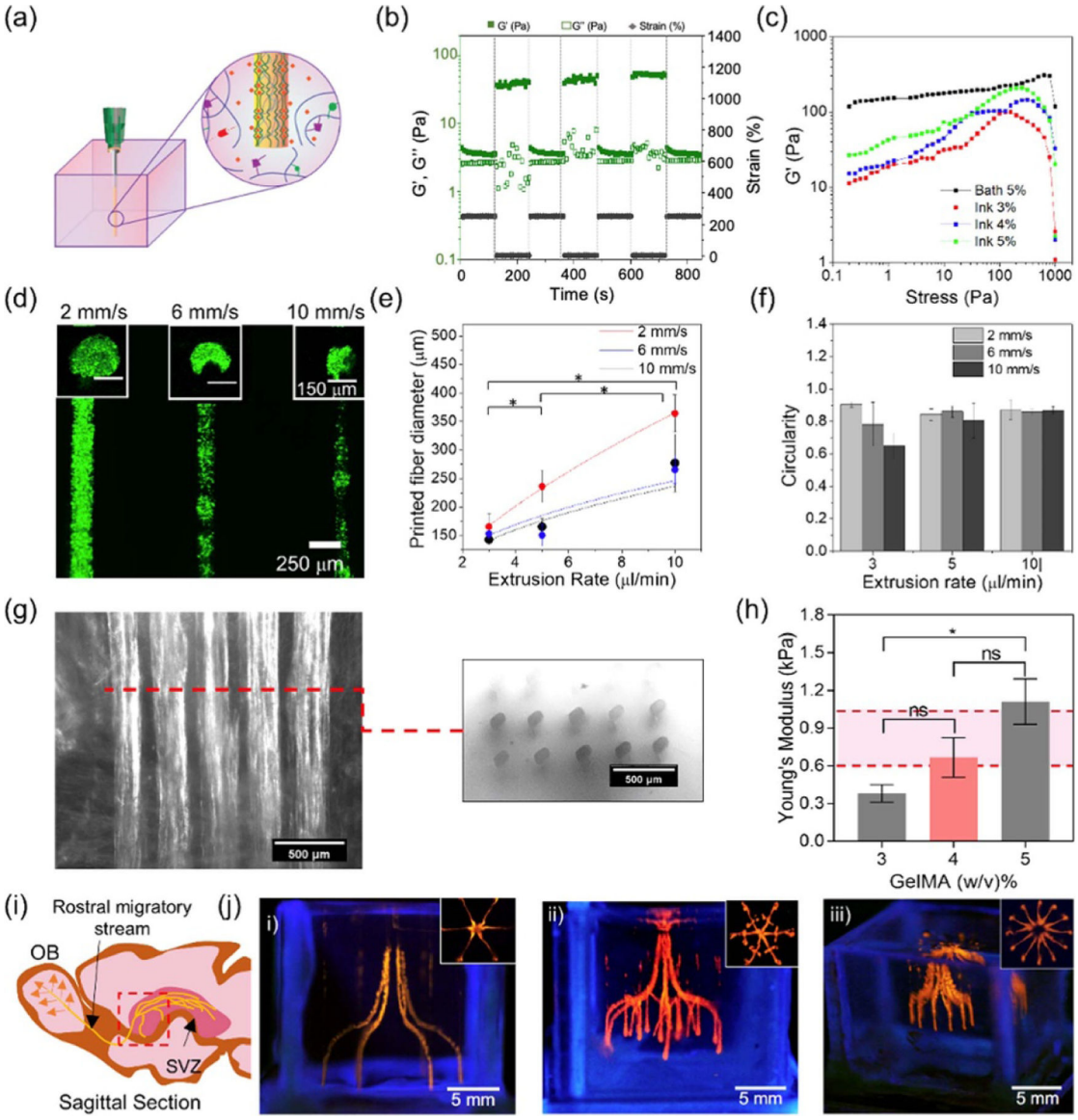

Figure 3.

Optimizing GGA bioinks. (a) Schematic diagram of the embedded bioprinted GGA bioink. (b) Oscillatory strain sweep between low (1%) and high (250%) strain shows the rapid phase transition from gel-like to fluid-like behavior of GGA bioink containing 4% GelMA (Ink 4%), necessary for localization of extruded bioinks ($n = 3$). (c) Oscillatory stress model shows the storage modulus (G') of bath-5% is higher than the other inks' conditions, suggesting that the 5% GelMA as a bath has the ability to maintain the fiber structure after printing. 3, 4, and 5% inks represent 3%, 4% and 5% GelMA in the GGA inks ($n = 3$). All bioinks in graphs b and c were measured at 25 °C. (d) The optical fluorescent image of the extruded fibers at different nozzle speeds and flow rates using a 30 G nozzle. (e) Diameter range, and (f) the circularity of printed fibers extruded from the 30 G nozzle in the supporting gel under various nozzle moving speeds and extrusion rates ($n = 3$). (g) Phase contrast imaging of the extruded parallel fibers with circular cross-sections and

approximately 300 μm thickness. (h) Young's modulus of the GGA ink containing different GelMA wt% concentrations. 3%, 4%, and 5% inks represent 3%, 4% and 5% GelMA in the GGA inks. The stiffness of our optimized condition (ink 4%) is in the range of the brain's stiffness ($n = 3$). (i) Schematic diagram showing the 3D geometry of the sagittal brain section and the rostral migratory system along with the olfactory bulb (OB) and subventricular zone (SVZ). The branched section denoted in red rectangle is modeled here using 3D bioprinting. (j) Different printed structures with various branch fibers showing a potential use for printing nerve fibers using our free-standing embedded printing technology.

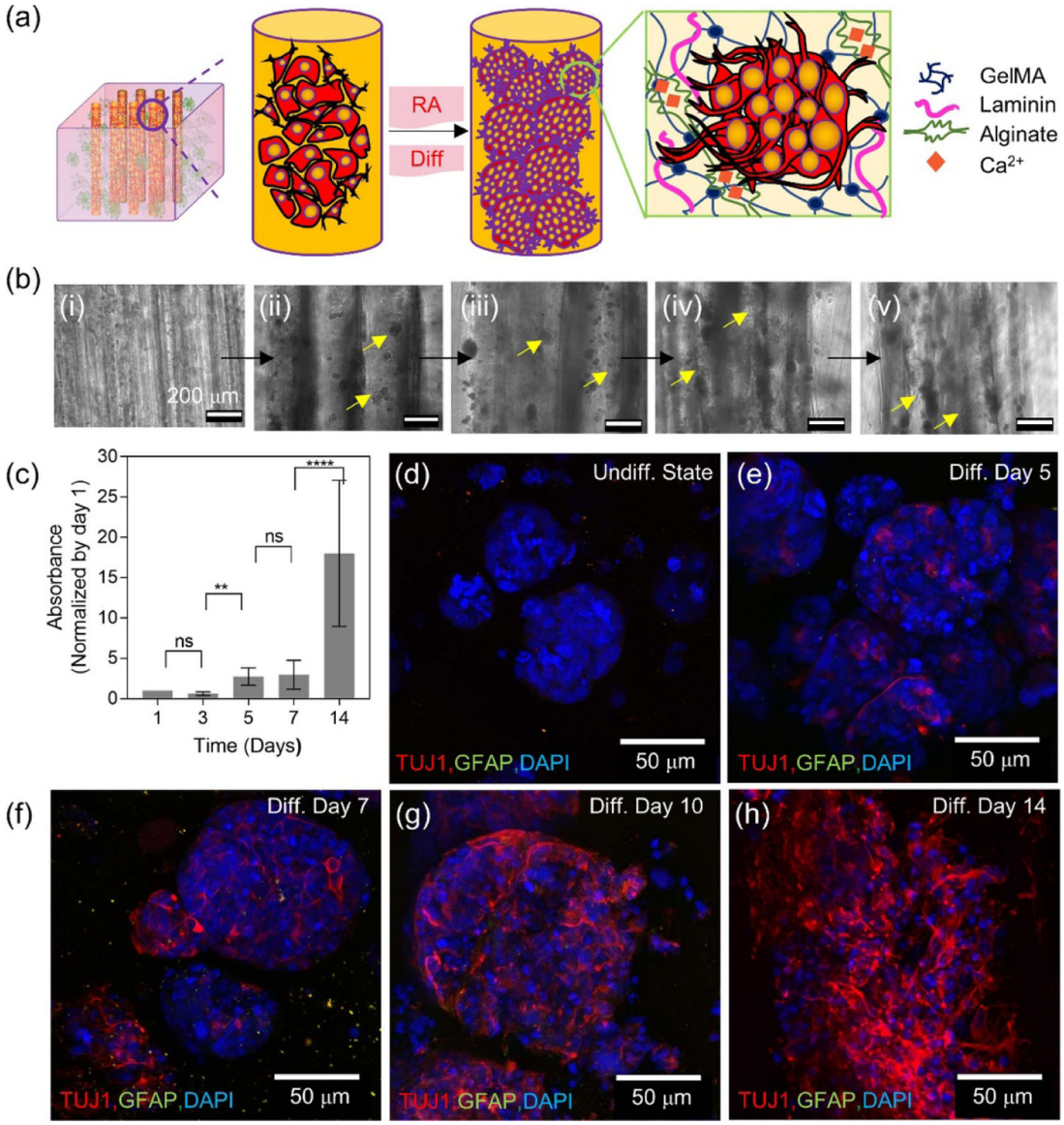

Figure 4.

Neuron-specific biomarker staining at different stages of differentiation. (a) Schematic diagram of the encapsulation, culture and differentiation processes of neural stem cells upon 3D bioprinting. (b) Optimizing the differentiation protocol for neuronal differentiation in 3D. RA in defined medium (MEM/F12, 1% ITS, P/S) was added for 48 h. At this stage, neural stem cells dominate the culture in dense planar sheets of culture (stage 1). After RA removal, dense aggregated colonies start to form in the culture (stage 2, b(i)). In 2D, these aggregates are loose and gradually detach from the surface, forming floating neural spheroids. In 3D, the spheroids form inside the printed fibers through migration and aggregation of cells (stage 3, b(ii)). After 7–8 d of *in vitro* culture, the aggregated spheroids settle in the 2D culture and attach to the surface followed by neurite formation (stage 4, b(iii)). Starting on day 10 of differentiation, the neurites and neural networks are formed in the 2D culture. In the 3D culture, the neurites and neural networks are formed across and

around the neuro-spheroids. Neurons are further matured by axonal development and high expression of specific biomarkers such as beta III tubulin (stage 5, b(iv)). If FBS-containing culture media is supplied to the culture, the neurites fasciculate and the population will gradually get populated by neuroglia (stage 6, b(v)). To avoid these conditions, neuron maturation media such as neurobasal medium or defined medium can be used. Scale bar in all images is 200 μm. (c) Metabolic activity of neural cell-laden bioink over the 14-d culture period ($n = 3$). (d) At stage 1 and before differentiation induction (undiff), neural stem cells dominate the population and no βIII tubulin expression is observed in the 3D neuro-spheroids. (e) Upon differentiation induction, some cells (~10%) start to show neuron biomarker expression. As the differentiation process progresses, the density of neurons in the culture is increased to (f) ~40% and (g) ~80% defining stage 5 of neuronal differentiation. (h) An interconnected spheroid network of neurons is observed in the printed nerve fibers after 14 d of differentiation, expressing positive βIII tubulin and negative GFAP, which shows successful differentiation of neural stem cells into neurons and not neuroglia.

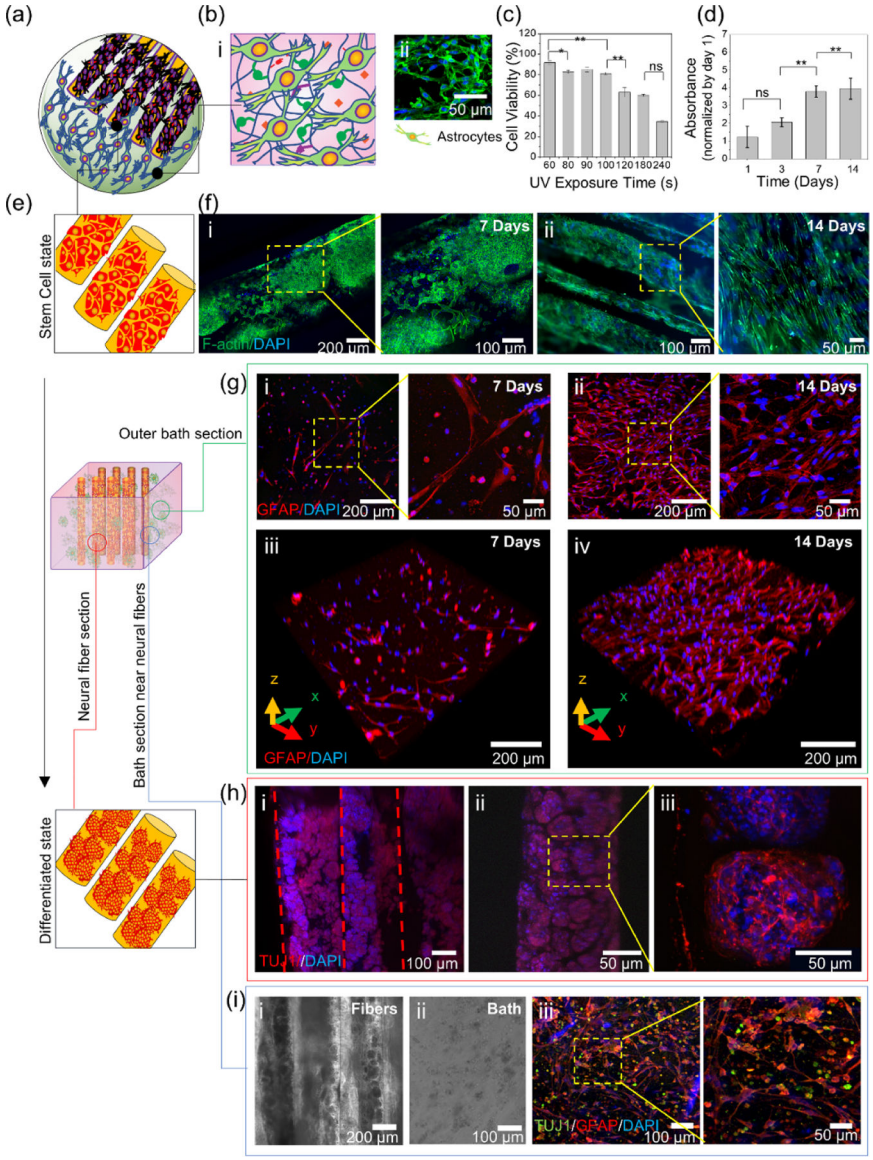

Figure 5.

Characterization of the 3D printed neural cell-laden bioink in the astrocyte-laden bath. (a) Schematic of the interface model of neural fibers in the astrocyte bath. (b–i) Schematic diagram of encapsulated astrocytes inside the GelMA bath. (b–ii) F-actin staining of the astrocyte-laden GelMA bath showing the structure of astrocyte networks inside the bath. (c) Cell viability of astrocytes in the 5% GelMA bath after UV treatment ($N = 3$). (d) Metabolic activity of astrocytes in the 5% GelMA bath over 14 d of *in vitro* culture ($N = 3$). (e) Printed fibers in undifferentiated states. (f) Fluorescent images of neural cell-laden fibers labeled by F-actin and DAPI after 7 (i) and 14 (ii) days of culture. (g) Outer bath area characterization. (i)–(ii) GFAP and DAPI staining of the astrocyte-laden baths 7 and 14 d after *in vitro* culture, confirming that the astrocytes could maintain a high metabolic activity, extend and form a network in the 5% GelMA bath. (iii)–(iv) 3D reconstruction of the GFAP/DAPI stained astrocyte-laden bath, acquired via Z-stack confocal imaging. (h) βIII tubulin (TUJ1)

and DAPI staining of the printed fibers (fiber boundaries shown in red, (h–i)) after 14 d of culture on day 10 of differentiation. (h–ii) and (h–iii) The morphologies of differentiated neuron cells in the printed fiber at a higher magnification field. (i) Co-culture of neuron and astrocyte cells labeled by TUJ1 and GFAP individually in the brain-like structures after 14 d of incubation. (i–i) and (i–ii) Phase contract images of the neuron and astrocyte cells in the printed fibers and bath. (i–iii) Immunostaining of co-cultured cells in the bath around the printed fibers.